Attractive interactions, molecular complexes, and polarons in coupled dipolar exciton fluids

C. Hubert,[1] K. Cohen,[2] A. Ghazaryan,[3] M. Lemeshko,[3] R. Rapaport,[2] and P. V. Santos[1,*]

[1]*Paul-Drude-Institut für Festkörperelektronik im Forschungsverbund Berlin eV., Hausvogteiplatz 5-7, 10117 Berlin, Germany*
[2]*Racah Institute of Physics, The Hebrew University of Jerusalem, Jerusalem 9190401, Israel*
[3]*IST Austria (Institute of Science and Technology Austria), Am Campus 1, 3400 Klosterneuburg, Austria*

Dipolar (or spatially indirect) excitons (IXs) in semiconductor double quantum well (DQW) subjected to an electric field are neutral species with a dipole moment oriented perpendicular to the DQW plane. Here, we theoretically study interactions between IXs in stacked DQW bilayers, where the dipolar coupling can be either attractive or repulsive depending on the relative positions of the particles. By using microscopic band structure calculations to determine the electronic states forming the excitons, we show that the attractive dipolar interaction between stacked IXs deforms their electronic wave function, thereby increasing the inter-DQW interaction energy and making the IX even more electrically polarizable. Many-particle interaction effects are addressed by considering the coupling between a single IX in one of the DQWs to a cloud of IXs in the other DQW, which is modeled either as a closed-packed lattice or as a continuum IX fluid. We find that the lattice model yields IX interlayer binding energies decreasing with increasing lattice density. This behavior is due to the dominating role of the intra-DQW dipolar repulsion, which prevents more than one exciton from entering the attractive region of the inter-DQW coupling. Finally, both models shows that the single IX distorts the distribution of IXs in the adjacent DQW, thus inducing the formation of an IX dipolar polaron (dipolaron). While the interlayer binding energy reduces with IX density for lattice dipolarons, the continuous polaron model predicts a nonmonotonous dependence on density in semiquantitative agreement with a recent experimental study [cf. Hubert *et al.*, Phys. Rev. X **9**, 021026 (2019)].

I. INTRODUCTION

The dipolar coupling is the dominating interaction mechanism between charge-neutral species. This interaction is presently receiving considerable attention due to its special properties. For two equal collinear dipoles with dipole moment $p\hat{\mathbf{z}}$ oriented along the $\hat{\mathbf{z}}$ direction in a medium with dielectric constant $\varepsilon\varepsilon_0$, the dipolar interaction energy can be expressed as

$$U_{dd}(\mathbf{r}) = \frac{p^2}{4\pi\varepsilon\varepsilon_0}\frac{(1 - 3\cos^2\theta)}{r^3}. \qquad (1)$$

Here, θ is the angle between the unit vector $\hat{\mathbf{z}}$ and the vector $\mathbf{r}$ connecting the two dipoles. The dipolar interaction has a long-range decay proportional to r^{-3} and is a nonmonotonic function of θ. Furthermore, the interaction strength depends not only on the magnitude of $\mathbf{r}$ but also on its orientation. In particular, the interaction between equal dipoles changes from repulsive to attractive for angles $\theta < \arccos[1/\sqrt{3}]$. This behavior contrasts to the Coulomb interaction between two equally charged particles, which is always repulsive and only depends on the distance between the particles.

The interplay between dipolar attraction and repulsion gives rises to interesting phenomena in dipolar fluids [1]. A typical example in classical systems is the formation of patterns in ferrofluids [2]. Recently, several investigations have

addressed dipolar interaction in ensembles of ultracold magnetic atoms and dipolar molecules. The anisotropic character of dipolar interactions affects the stability and determines the shape of clouds of atomic dipolar [1,3]. Due to the attractive dipolar component, the dispersion relation for density fluctuations in these systems can exhibit a roton-maxon feature characterized by a local minimum for nonzero wave vectors [4,5]. Under appropriate conditions, instabilities around these local minima can induce the symmetry break leading to the formation of self-organized droplet crystals [2]. Recently, these systems have been also shown to exhibit supersolidity, the combination of spatial ordering with superfluidity [6–9].

In the solid state, promising systems for the investigation of the coupling between mobile dipoles include excitons in bilayer electron systems [10,11] and spatially indirect excitons (IXs) in semiconductor double quantum well (DQW) structures [see Fig. 1(a)] [12–14]. The latter consists of two QWs separated by a thin tunnel barrier (i.e., with a thickness much smaller than the exciton Bohr radius). The DQWs are normally inserted within the intrinsic region of a reversed bias p-i-n junction to allow the application of a transverse electric field $F_z\hat{\mathbf{e}}_z$, as shown for an (Al,Ga)As structure in Fig. 1(a). Field-induced tunneling drives photoexcited electrons and holes to different QWs, thus creating excitons with a permanent dipole moment $p\hat{\mathbf{e}}_z$ oriented anti-parallel with respect to the field direction.

Most studies of IX dipoles have been restricted to particles confined in a plane perpendicular to their dipole orientation.
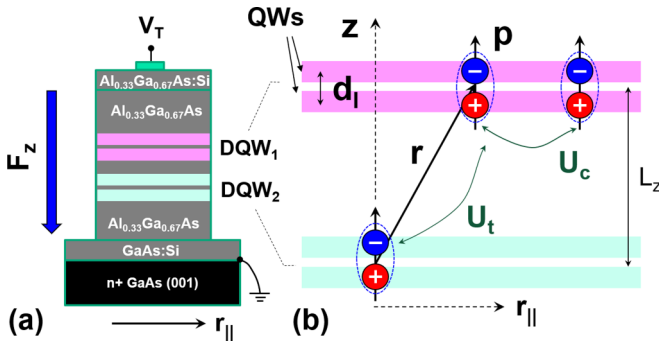
*santos@pdi-berlin.de

FIG. 1. Dipolar interaction between indirect excitons (IXs) in stacked double quantum wells (DQWs). (a) DQWs consisting of GaAs QWs separated by a thin $Al_{0.3}Ga_{0.67}As$ barrier are inserted within the intrinsic region of a reversed-biased Schottky diode subjected to a voltage V_T. The associated electric field F_z induces the formation of IXs with dipole moment **p** under optical excitation. (b) Intra-DQW (U_c) and inter-DQW (U_t) dipolar interaction between two IXs.

In this configuration, the inter-IX interactions are only of repulsive nature. Recently, we have proposed and demonstrated a concept to access the attractive dipolar coupling between IXs using stacked DQWs [see Fig. 1(b)] [15]. These configuration enables the orientation of dipoles with angles $\theta < \arccos[1/\sqrt{3}]$. The barrier between the two DQW bilayers was chosen to be sufficiently large to prevent single-particle tunneling but small enough to allow for electrostatic coupling between them. Under these conditions, the attractive inter-DQW dipolar interaction becomes sufficiently strong to induce density correlations and dragging between IX clouds in the two DQW bilayers. In addition, the inter-bilayer binding energies was determined from the energetic shifts of the photoluminescence lines from the interacting IX clouds. Interestingly, the latter was found to increase with bilayer density up to densities of approx. 5×10^{10} cm^{-2}, where it reaches values exceeding 5 meV, and then to decrease for higher densities (cf. Fig. 6 of Ref. [15]). It is interesting to note that depending on density, the interlayer binding can thus be comparable to the intralayer IX binding energy in GaAs QWs.

In a previous theoretical study [16], we have calculated the interlayer binding energy of an IX molecule consisting of two IXs, each in one of the DQW bilayer. This binding energy for the sample used in Ref. [15] reaches only a few tens of μeV and is thus much smaller than the measured interlayer binding energies. The calculations were carried out using the point charge approximation (PCA), which assumes that the electrons and holes constituting the IX to be described as point charges located at the center of the QWs. They neglect, therefore, the internal charge distribution within the dipolar species. The PCA is a very good approximation for diluted gases of atomic and molecular dipoles, where the dipolar field can be considered slowly varying over the length of the dipoles. It may fail, however, when the interdipolar distances become comparable to the length of the dipoles.

In this work, we theoretically investigate the dipolar coupling between single IXs as well as multiple IXs, thus also including many particle effects not previously addressed for DQW bilayers. Due to the different degrees of complexity and length scales, the problem is addressed using different techniques. We first analyze the dipolar coupling beyond the PCA approximation by addressing the coupling between extended dipoles with interdipolar separations comparable to the dipole lengths. For that purpose, we have carried out self-consistent calculations of the energy and wave functions of electrons and holes for the system of two interacting IXs shown in Fig. 1(b). The wave functions were determined using the tight-binding (TB) approach to be described in Sec. II. This method enables the determination of the distortion of the wave functions induced by the applied electric field, which makes the dipole moments field-dependent (Sec. III B). We have also applied the TB method to account for modifications of the potential in one DQW induced by the presence of an IX in the other DQW. We show that polarization effects induced by the interaction between two IXs lead to non-negligible corrections to the binding energy of IX molecules as well as of indirect trions, as is described in detail in Sec. III C.

The large interlayer binding energies reported in Ref. [15] were measured in an IX density regime, where the average separation between IXs within a DQW-bilayer is comparable to the separation between the bilayers, thus indicating that they may arise from many-body interaction effects, which are addressed in Sec. IV. Here, we start by considering the coupling between a single dipole in one DQW bilayer with a cloud of dipoles in the adjacent DQW (Sec. IV A). The dipoles in the cloud are assumed to be arranged in a regular lattice. We show using an electrostatic model that the lattice dipolar interaction energy reduces with the lattice density. This model is complemented by an exact diagonalization model (Sec. IV B) for the interaction between one-dimensional (1D) dipolar bilayers, which predicts the experimentally observed minimum of the interlayer binding energy for equal IX densities in the two DQW bilayers. The IX interlayer binding energies predicted by the lattices models are, however, much smaller than the measured ones.

The last sections are devoted to dipolaron models for the interlayer interaction. We first demonstrate that the local deformation of the lattice due to the coupling to a single IX in a remote DQW can lead to the formation of a dipolaron, which further increases the IX interlayer binding energy (Sec. IV C 1). The lattice dipolaron corrections to the interlayer binding energies are, however, very small. Finally, Sec. IV C 2 introduces a continuous model for a Fröhlich-type dipolarons based on an interaction Hamiltonian, which can be exactly diagonalized. An analogous treatment has been recently proposed for dipolar cold atoms [17]. Preliminary results for dipolaron in coupled DQW bilayers have been presented in Ref. [15]. This model allows us to address the impact of interactions within the IX fluids on the dipolaron formation energy. Its predictions depend on the correlation state of the IX gas. In the low density regime, where correlations are not expected to be important, the interlayer binding energy increases with the gas density. As the density increases, one expects a transition to a correlated regime, where the interlayer binding energy is small and reduces with density. This behavior is in qualitative agreement with the predictions of the lattice model, which implicitly assumes correlated species. The dipolaron model also semi-quantitatively

describes the density dependence of the interlayer binding energies reported in Ref. [15]. The main conclusions are summarized in Sec. V.

II. CALCULATION PROCEDURE

We have investigated the prototype structure sketched in Fig. 1 consisting of two DQWs, each formed by two 10-nm-wide (001) GaAs QWs separated by 4-nm-wide outer $Al_{0.3}Ga_{0.7}As$ barriers. The DQWs are separated by a 10-nm-thick $Al_{0.3}Ga_{0.7}As$ barrier thus yielding a vertical separation between the DQW centers of $L_z = 34$ nm [cf. Fig. 1(b)].

Equation 1 yields the electrostatic interaction energy between two IXs in the PCA in the far field. Since the vertical separation between the dipoles is only a few times larger than the dipole length d_l for the studied sample, we have used for the determination of the interactions the full expression for the electrostatic energy between four charged particles given by

$$U_{dd}^{(c)}(\mathbf{r}) = \frac{e}{4\pi\varepsilon\varepsilon_0}\left(-\frac{1}{\sqrt{(d_l + L_z)^2 + r_\parallel^2}}\right.$$
$$\left. -\frac{1}{\sqrt{(L_z - d_l)^2 + r_\parallel^2}} + \frac{2}{\sqrt{L_z^2 + r_\parallel^2}}\right). \quad (2)$$

Here, e is the electron charge, $\epsilon = 12.9$ the effective dielectric constant of the layer structure, and $d_l = p/e$ the length of the dipoles. The first two terms within the parenthesis arise from the attractive interaction between the IX charges of opposite signs in DQW_1 and DQW_2, while the last one accounts for the repulsion between charges of the same sign.

The electronic structure of the IXs was determined using the empirical TB method [18]. The simplicity of the TB method enables the microscopic determination of the band structure of DQWs with QW widths up to a few tens of nm using moderate computational efforts. Although empirical in the sense that it uses parameters fitted to the bulk band structure, it can be regarded as "microscopic" when compared with other approaches such as the $\mathbf{k} \cdot \mathbf{p}$ effective mass calculations. The TB calculations used a basis consisting of sp^3s^* orbitals [19] including spin-orbit coupling [20,21]. This orbital basis consists of 10 orbitals per atom and includes only nearest-neighbor interaction. It has been shown to reproduce well the highest valence and the lowest conduction bands of most bulk semiconductors [19].

The TB calculations were carried out for a periodic supercell consisting of a single DQW sandwiched between two 8-nm wide $Al_{0.3}Ga_{0.7}As$ outer barriers. The TB parameters employed for the GaAs and $Al_{0.3}Ga_{0.7}As$ layers are summarized in Table I. The effects of the external electric field F_z were taken into account by adding the position-dependent electrostatic energy to the on-site TB parameters. A similar procedure was used to address IX–IX interactions, as will be described in detail in the next sections.

TABLE I. TB parameters (in units of eV) used in the calculation of IX interactions. The notation used correspond to the one of Ref. [22]. In order to account for the valence band discontinuity we subtracted 0.16 eV from the diagonal parameters (i.e., E_s, E_p, and E_{s*}) of the $Al_{0.3}Ga_{0.7}As$ layers.

Parameter	GaAs[23] (eV)	$Al_{0.3}Ga_{0.7}As$ (eV)
E_s(anion)	−8.457	−8.1774
E_p (anion)	0.9275	0.93125
E_s(cation)	−2.7788	−2.29466
E_p (cation)	3.5547	3.55029
V_{ss}	−6.4513	−6.51511
V_{xx}	1.9546	1.94782
V_{xy}	4.77	4.6122
V_{sp}(anion,cation)	4.48	4.6672
V_{sp}(cation,anion)	7.85	7.1378
E_{s*}(anion)	8.4775	8.17915
V_{s*p}(anion,cation)	4.8422	4.73714
E_{s*}(cation)	6.6247	6.65539
V_{s*p}(cation,anion)	7	6.3988
$3\lambda_a$ (anion)	0.39	0.39342
$3\lambda_c$ (cation)	0.174	0.129

III. SINGLE IX INTERACTIONS

A. Exciton-exciton interactions

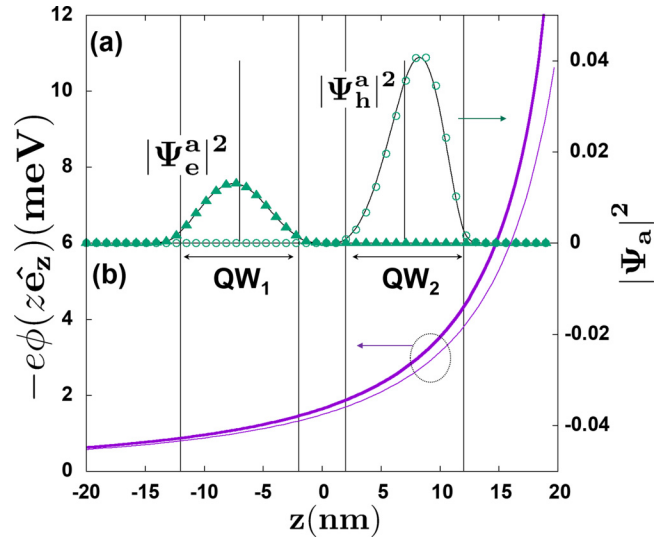The thin line in Fig. 2 displays the spatial dependence of the TB wave functions (more precisely, the squared wave

FIG. 2. (a) Squared tight-binding wave functions projected on the anion sites (superscript a) for the lowest conduction ($|\Psi_e^a|^2$) and highest valence band state $|\Psi_h^a|^2$ calculated for an applied field $F_z = 20$ kV/cm (thin lines). The symbols show the corresponding wave functions obtained using the self-consistent approach to take into account for the presence of an IX in the adjacent DQW (see text for details). (b) Spatial dependence of the electronic potential energy $[-e\phi(z)]$ generated by the IX in DQW_2 on the atomic sites of DQW_1 [cf. Fig. 1(b)] for zero lateral separation x as determined using the self-consistent TB approach. The thin line shows the corresponding potential for DQW_2 calculated in the point charge approximation.

function envelopes) of the lowest conduction band state $|\Psi_e^a|^2$ and highest valence band state $|\Psi_h^a|^2$ calculated for a single DQW under an applied field $F_z = 20$ kV/cm. The electron and hole wave functions are normalized according to $\int_{-\infty}^{\infty} |\Psi_{e(h)}^a|^2 dz = 1$. For clarity, we only show the projection of the wave function on the anion sites (superscript a). The larger amplitudes for holes than for electrons reflect the fact that the hole wave functions for the band-edge states have higher amplitudes on the anion sites (the opposite applies for the cation sites). The applied electric field makes the electron and the hole wave functions asymmetric with a center of mass shifted with respect to the center of the QWs. Note that the electron and hole wave functions shift in opposite directions under the applied field, thus increasing the electric dipole moment of the IX species.

The interaction energy between two IXs [IX$_1$ and IX$_2$ located in DQW$_1$ and DQW$_2$, respectively, cf. Fig. 1(b)], was calculated using the following self-consistent approach. First, the TB wave functions calculated for one DQW (assumed to be DQW$_2$) were used to determine the charge distribution along the z direction in the location of the remote DQW (DQW$_1$). The latter was then applied to correct the on-site electronic potentials ($\Delta\phi(r_\parallel, z_{i,1})$) on the neighboring DQW according to

$$\Delta\phi(r_\parallel, z_{i,1}) = \frac{e}{4\pi\epsilon\epsilon_0} \sum_{z_{j,2}} \left[\frac{|\Psi_{h,2}(z_j,2)|^2 - |\Psi_{e,2}(z_j,2)|^2}{\sqrt{r_\parallel^2 + (L_z + (z_{j,2} - z_{i,1}))^2}} \right].$$

(3)

Here, the subscripts 1 and 2 denote, respectively, the coordinates across the IX structures in DQW$_1$ and DQW$_2$. The energy eigenvalues and the wave functions for DQW$_1$ were then calculated under the corrected potential. This procedure was then repeated until self-consistency was reached, as defined by changes in $\Delta\phi$ in successive iteration steps of less than 10^{-5} eV. In general, the procedure converges after a few iteration steps.

The symbols in Fig. 2 show the self-consistent electron and hole wave functions for two coupled DQWs under the interaction potential given by Eq. (3). The shape of the wave functions is very similar to the ones for IXs in an uncoupled DQW (thin line), except for the slightly larger shifts with respect to the center of the QWs (the shifts are smaller than the size of the symbols for $|\Psi_{e(h)}^a|^2$). The latter translates into a slightly enhanced IX electric dipole moment. The thick solid line in the lower panel of the figure displays the spatial dependence of the self-consistent potential $\phi_e(x = 0, z_{i,1})$. The dashed line shows, for comparison, the dipole potential calculated in the PCA. In both cases, the electronic potential increases towards positive z due the presence of the second dipole centered at $z = \ell_z$ [cf. Fig. 1(b)]. The slightly larger values for the self-consistent potential arise from the extended character of the wave functions as well as from the distortions of the wave functions induced by the remote IX dipole.

The potential interaction energies $U_c(x, L_z = 0)$ and $U_t(x, L_z)$ for an IX molecule as well as for two IXs in the same DQW, respectively, can be determined as the difference between the self-consistent TB transition energies and the one
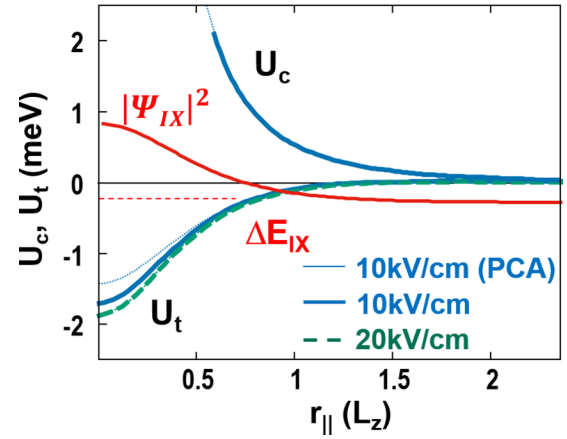

FIG. 3. Interaction energy between two IXs in the same (U_c) and in different DQWs (U_t) as a function of their lateral separation (in units of $L_z = 34$ nm). The calculations for U_t were carried out for electric fields F_z of 10 and 20 kV/cm. The thin line displays U_t as determined in the point charge approximation of Ref. [16]. The horizontal dashed line marks the interlayer binding energy of the single IX molecular state confined in this potential, ΔE_{IX} (calculated for $F_z = 10$ kV/cm). The corresponding wave function amplitude $|\Psi_{IX}|^2$.

for an isolated IX. The dependence of these energies on lateral separation $r_\parallel$ is plotted in Fig. 3. As expected, the intra-DQW interaction is always repulsive and stronger in magnitude than the inter-DQW one. The thin line represents for comparison the dipolar energy determined in the PCA (cf. Ref. [16]) for an electric field $F_z = 10$ kV/cm. As expected, the minimum energy configuration corresponds to two stacked IXs (i.e., with lateral separation $r_\perp = 0$).

The self-consistent interaction energy U_t is approximately 20% larger than the corresponding one ($\Delta U_{t,PCA}$) from the PCA. This inter-DQW polarization behavior can be understood with the help of Fig. 2. In the PCA, the interaction energy $U_{t,PCA}$ is simply given by the difference between the electrostatic potentials $|-e\phi_{t,PCA}|$ (thin line) at the center of the two QWs. The self-consistent electron and hole TB wave functions, in contrast, extend over the width of the QWs and also penetrate the barriers. The deformation of the wave functions together with the strong z dependence of $-e\Delta\phi(x, z)$ ($\approx r^{-3}$) shift the energies of the electron and hole eigenstates towards opposite directions, thus increasing the IX interlayer binding energy.

The deformation of the wave functions makes the IX dipole moment dependent on the applied field. The impact of the field polarizability becomes evident when one compares the field-induced changes $\Delta E_{IX}^{(f)}$ of the resonance energy of an IX-IX molecule with the one of an isolated IX, as illustrated, respectively, by the solid and dashed lines in Fig. 4.

Finally, the binding potential between remote IXs determined using the TB calculations presented here (as well as in the following sections) only takes into account the effects of the remote dipolar coupling on the electronic potential at the location of the QWs. It neglects, therefore, the impact of the remote dipolar coupling on the overlap between the electron and hole wave functions, which determine the binding energy of IXs in a DQW [24]. This approximation
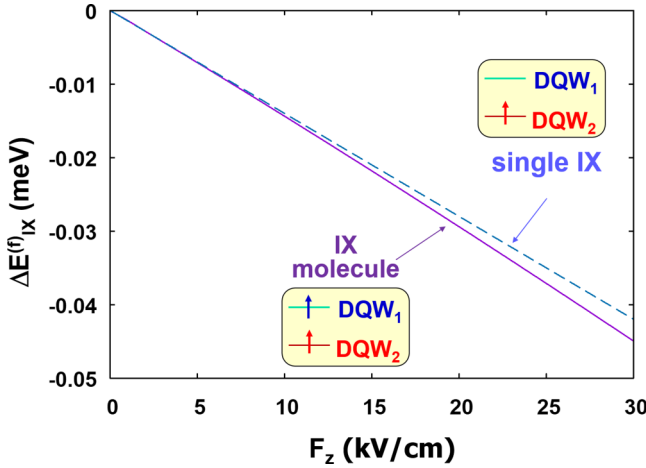
FIG. 4. Electric-field-induced changes $\Delta E_{IX}^{(f)}$ of the resonance energy of a single IX (dashed line) and of an IX-IX molecule (solid line).
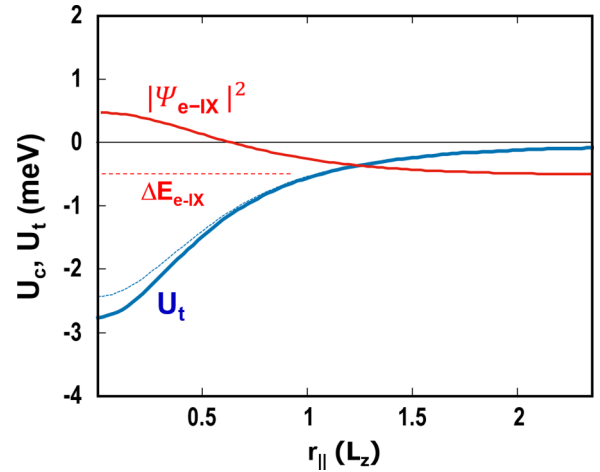

FIG. 5. Interaction energy U_t between an indirect trion e-IX consisting of an IX in one DQW and an electron in the adjacent DQWs as a function of the lateral separation $r_\parallel$ calculated for $F_z = 10$ kV/cm. The dashed line displays U_t determined in the point charge approximation of Ref. [16]. The horizontal dashed line marks the energy of the single confined state in this potential, ΔE_{e-IX}. The corresponding wave function amplitude $|\Psi_{e-IX}|^2$ is also displayed.

is justified by (i) the small IX binding energy in the present samples (less than 3 meV, as estimated from the calculations in Ref. [24]) and (ii) the negligible modifications of the electron and hole wave functions changes induced by the remote dipolar coupling (cf. Fig. 2).

B. Molecular binding energy

The attractive inter-DQW potential U_t of Fig. 3 can bind two IXs to form an IX molecule. In order to obtain the molecular binding energy, one also needs to take into account the kinetic energy arising from motion of the bound IX dipoles in the DQW plane. We followed, for that purpose, a procedure introduced in Ref. [16], which consists in numerically solving the Schrödinger equation for the relative motion of an IX-IX pair under the radial potential $U_t(r)$ [25]. The calculations were carried out assuming a reduced effective mass for the IX molecule equal to the combined mass of the electron (m_e) and heavy-hole (m_{hh}) in GaAs, i.e., $\frac{1}{2}(m_e + m_{hh})$ with $m_e = 0.067$ and $m_{hh} = 0.22$. In agreement with Ref. [16], we found that the inter-DQW potential supports a single bound state with zero angular momentum and energy ΔE_{IX} and wave function $|\Psi_{IX}|^2(r)$ displayed in Fig. 3. It is interesting to note that the strong kinetic corrections due to the small reduced mass and short extension of the attractive potential yields an interlayer binding energy $\Delta E_{IX} = 0.28$ meV much smaller than the potential depth $U_t(r_\parallel = 0) = -1.7$ meV determined for $F_z = 10$ kV/cm.

The shape of the inter-DQW potential $U_t(r)$ may be affected by lateral (i.e., along the DQW plane) distortions of the electron and hole wave functions induced by IX-IX interactions, which cannot be addressed using the 1D TB approach employed here. We have estimated the impact of these distortions in the PCA approximation by assuming that the electron and the hole charges can be displaced by small amounts $-\Delta r$ and Δr, respectively, in order to minimize the electrostatic interaction energy between two IXs (note that such a distortion does not change the electrostatic energy associated with the vertical field F_z). We found that $U_t(\Delta r, r_0)$ can indeed be minimized by a nonvanishing Δr. The energy reduction (on

the order of a few tens of μeV) and magnitude of the shifts ($|\Delta r| < 0.5$ nm), however, are too small to introduce sizable corrections to $U_t(r)$ or to the interlayer binding energy.

C. Indirect exciton-carrier interactions

IXs in one DQW can also couple to an electron or a hole in the other DQW to form a spatially indirect trion. We have extended the TB approach to estimate the interlayer binding energy of these species. The procedure is essentially the same as the one used in the previous section, except that we neglect the hole charge distribution in one of the DQWs [e.g., $\Phi_{h,2}$ in Eq. (3)]. The results for the interaction of an IX in DQW$_1$ with an electron in the lower QW of DQW$_2$ (cf. Fig. 1) are summarized in Fig. 5. When compared to the inter-DQW attractive potential $U_t(r)$ between two IXs of Fig. 3, the electron-IX interaction is approximately 50% stronger has also a longer lateral decay length. This potential supports a bound state with an interlayer binding energy $\Delta E_{e-IX} = 0.53$ meV almost twice as large as the one for an IX molecule. Similar results apply to hole trions. The interaction of trions with the electric field is also increased by approximately 33%.

IV. MANY-PARTICLE EFFECTS

The inter-DQW binding energy for the remote interactions between two IXs determined in the previous section are larger compared to the values obtained in the PCA but still much smaller than the one measured in Ref. [15]. This discrepancy has motivated us to analyze dipolar interaction effects involving many particles.

A. Indirect exciton lattices

The previous results for the inter-DQW dipolar interaction apply for low IX densities, i.e., when the average separation
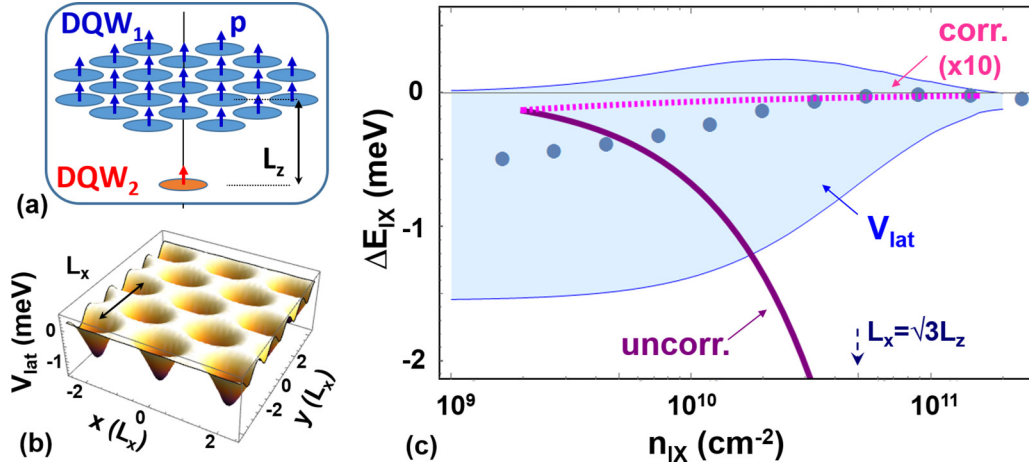
FIG. 6. (a) Interaction between a single IX in DQW$_2$ with a closed-packed IX lattice in DQW$_1$. (b) Dipolar potential on the single IX in DQW$_2$ induced by the lattice in DQW$_1$ with a lattice constants $L_x = 2L_z$ and density $n_{IX} = 2/(\sqrt{3}L_x^2)$. (c) Shaded region: Range of the local dipolar interaction potential [V_{lat}, cf. Eq. (4)] experienced by the single IX in (a) as a function of lattice density. The superimposed dots are the lowest energy IX quantum state in this potential, which correspond to the IX interlayer binding energy (ΔE_{IX}). The vertical dashed arrow marks the density for which $L_x = \sqrt{3}L_z$. The thick dotted and solid lines display the prediction of the continuous dipolaron model in the limit of fully correlated [corr., cf. Eq. (17)] and uncorrelated [uncorr., cf. Eq. (18)] IX gases, respectively.

L_x between IXs within a DQW far exceeds the distance L_z between the DQWs. For larger densities, multiparticle interaction effects modify the inter-DQW interaction potential with respect to the simple form given by Eq. (1). In order to make the many-body problem tractable, we first neglect kinetic effects and assume that the high-density IXs are arranged in a regular lattice. We note that since dipolar interactions fall rather quickly with increasing distance, mostly contributions of nearest and next-nearest neighbors are important. This means that ordered lattice models also approximate a correlated liquid with only short-range order [26,27]. A stable lattice configuration requires an isometric lattice (e.g., a square, triangular or hexagonal lattice). We have opted for a triangular lattice, since it provides the maximum number of nearest neighbors [28]. Specifically, we have considered the configuration illustrated in Fig. 6(a), where a single IX in DQW$_2$ interacts with a triangular lattice of IXs generated by the lattice vectors $\mathbf{v_a} = (1, 0)L_x$ and $\mathbf{v_b} = (\sqrt{3}/2, 1/2)L_x$, where L_x is the lattice constant. The particle density n_{IX} in the triangular lattice is related to the lattice constant L_z according to $n_{IX} = 2/(\sqrt{3}L_x^2)$.

The dipolar potential V_{lat} experienced by the single IX can be obtained by assuming that the electrons and holes forming the dipoles in the lattice to be elementary point charges located at the center of the respective QWs in the stacked DQW structure. For an IX at position $\mathbf{r} = (\mathbf{r}_\parallel, r_\perp)$, where $\mathbf{r}_\parallel$ and $\mathbf{r}_\perp$ are the in-plane and out-of-plane displacement components, respectively, the potential is calculated by summing the $U_{dd}(\mathbf{r})$ contributions [cf. Eq. (2)] summed over the lattice sites. The potential $V_{lat}(\mathbf{r})$ experienced by the single IX in DQW$_2$ then becomes

$$V_{lat}(\mathbf{r}_\parallel, \mathbf{r}_\perp) = \sum_{i,j}^{\mathbf{r}_\parallel < r_{max}} U_{dd}^{(c)}[\mathbf{r}_\perp - |i\mathbf{v_a} + j\mathbf{v_b} + \mathbf{r}_\parallel|]. \quad (4)$$

Due to the extended nature of the potential, the summation needs to be carried out over a large number of lattice around the central IX in order to ensure convergence. In order to reduce the computational efforts, the coupling to lattice IXs at lateral distances $r_\parallel > r_{max} \approx 20 L_x$ was taken into account by replacing the summation in Eq. (4) by an integration over a continuous density of dipoles.

Figure 6(b) displays the potential experienced by the single IX as it moves underneath a lattice with lattice constant $L_x = 2L_z$. For $L_x \gg L_z$, the potential V_{lat} around each site resembles the one for the dipolar potential U_{dd} with the minima of the potential aligned with the lattice sites. The shaded region in Fig. 6(c) marks the energy range spanned by the lattice potential $V_{lat}(\mathbf{r})$. In the opposite limit $L_x \ll L_z$, $V_{lat}(\mathbf{r}) \to 0$, thus reproducing the well-known result that the electric field generated by an infinite sheet of dipoles vanishes at large distances. The minima of $V_{lat}(\mathbf{r})$ are always higher than the potential $U_t(0)$ for a single IX-IX pair [cf. Fig. 3]; this model thus predicts a reduction of the IX interlayer binding energy with increasing lattice density. The last behavior arises from the dominating contribution of repulsive intra-DQW interactions with increasing densities.

The quantum corrections required for the determination of the interlayer binding energy of the single IX to the lattice were determined by numerically solving the 2D Schrödinger equation for a IX in the periodic lattice potential. The dots in Fig. 6(c) display the density dependence of the lowest energy level ΔE_{IX}. In the limit of small densities, the interlayer binding energies $|\Delta E_{IX}|$ are larger than the ones for an IX molecule (cf. Fig. 3). The latter is due to the fact that the lattice is assumed to be static, so that the kinetic energy of the particle becomes equal to the IX mass (rather than to reduced mass of two IX, as in the case of an IX molecule). Note again that the absolute values for the interlayer binding energies are smaller than the depth of the interaction potential.

B. Exact-diagonalization study of IXs

In this section we analyze many-particle effects employing a numerical exact-diagonalization method. This method is quite powerful in capturing long-range correlations, although it suffers from small system size effects. In order to be able to consider significantly larger systems, in this section we limit the discussion to 1D systems. Namely, we consider two double quantum wire structures with parameters similar to the full two DQWs case.

Since exact diagonalization requires finite Hilbert space, we assume that IXs occupy sites of an artificial IX lattice. It should be noted that the notion of a lattice in this section is different from the one considered in the other sections of the paper, where the single IXs are fixed at the lattice sites. Here, in contrast, the IXs can hop between different lattice sites and multiple occupation of each site is allowed. Introduction of the artificial lattice and of a cutoff length scale (introduced below) accounts for short wavelength processes, which are considered only at the phenomenological level in the current treatment. The kinetic energy of the IXs is included as terms of nearest neighbor hopping. We construct the supercell of the size $L_x^T = nL_x$, where L_x in this section denotes the lattice constant of the artificial lattice. In order to mimic infinite lattice and isolate bulk physics from edge effects, we apply periodic boundary conditions to the supercell. This modifies the form of the interaction potential given by Eq. (1) of the main text, because now the IX interacts both with the IXs in the supercell, as well as with the images of the IXs in other supercells. The modified interaction has the form

$$U^{PBC}(x) = \sum_{s=-\infty}^{+\infty} \mu^2 \frac{(1 - 3\cos^2\theta_s)}{r_s^3}, \quad (5)$$

where

$$\mu = p/\sqrt{4\pi\varepsilon\varepsilon_0}. \quad (6)$$

For the intralayer interaction $\theta_s = \pi/2$ and $r_s^2 = a^2 + x_s^2$ whereas for interlayer interaction $\cos\theta_s = L_z/r_s$ and $r_s^2 = x_s^2 + L_z^2$. Here $x_s = x + sL_x^T$. The cutoff length scale a is introduced to remove the divergence of the intralayer interaction when two IXs occupy the same site. Introduction of the cutoff phenomenologically accounts for the fact that dipolar interaction will be modified when the separation between IXs becomes comparable to the IX effective dipole length. While the modified interaction has a complex form in real space, the Fourier transform is less cumbersome

$$U_{intra}^{PBC}(k) = 2\mu^2 \frac{|k|}{a} K_1(|k|a), \quad (7)$$

$$U_{inter}^{PBC}(k) = 2\mu^2 \left(\frac{|k|}{L_z} K_1(|k|L_z) - k^2 K_2(|k|L_z) \right), \quad (8)$$

where $K_i(x)$ is the modified Bessel function of the second kind.

Once the Hamiltonian is formed we construct the full Hilbert space for a small number of particles and diagonalize the resulting Hamiltonian matrix. The diagonalization can be carried out both in real and momentum space. In real space the interaction expressed by Eq. (5) is diagonal, whereas in momentum space the kinetic term will be diagonal. We
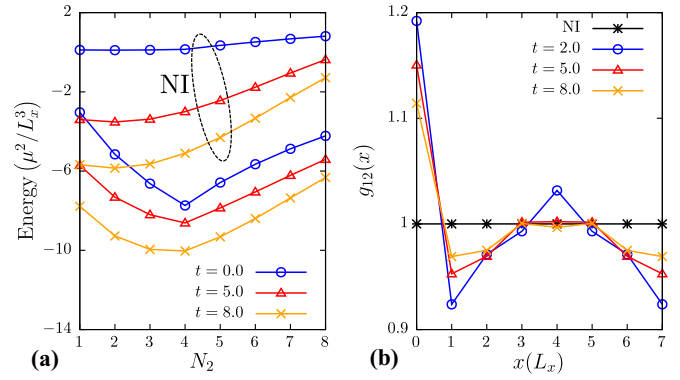

FIG. 7. (a) Dependence of the energy per IXs on number of IXs in the second layer when $N_1 = 4$ for different values of the hopping amplitude. (b) interlayer pair correlation function $g_{12}(x)$ for different values of hopping amplitude. Dashed lines in both figures correspond to the case when there is no interlayer interaction (NI stands for no interlayer interaction).

mostly work in momentum space, where the kinetic term takes the standard form $H_0(k) = t\cos(kL_x)$, where t is the hopping amplitude. After diagonalization, the evaluated wave functions can be used to calculate physical properties of the ground state, such as pair correlation functions and static structure factors. Using the translational invariance of the system the pair-correlation function can be stated in the form:

$$g_{l'l}(x) = \frac{1}{N_{l'}N_l} \sum_{k_1,k_2,k_3,k_4} \delta_{k_1+k_2,k_3+k_4} e^{i(k_1-k_2+k_3-k_4)\frac{x}{2}}$$
$$\times b_{l'k_1}^\dagger b_{lk_2}^\dagger b_{lk_3} b_{l'k_4}, \quad (9)$$

where the index l and l' denote the dipole layer (1 or 2), N_l is the total number of IXs in layer l and $b_{l'k}^\dagger$, $b_{l'k}$ denote, respectively, the creation and annihilation operators for the state k in layer l. Similarly, for the structure factors we have

$$S_{ll'}(q) = \frac{1}{N} \rho_l(q)\rho_{l'}(-q) - \frac{N_l N_{l'}}{N} \delta_{q0}, \quad (10)$$

where q is the wave vector, $N = N_1 + N_2$ is the total number of IXs and $\rho_l(q) = \sum_k b_{lk}^\dagger b_{lk-q}$ is the Fourier transform of the density operator.

The calculated energies will be presented in units of μ^2/L_x^2 and the lengths will be normalized to L_x. The used parameters are $L_z = 0.5$, $a = 0.2$, $L_x^T = 10$, which correspond to ones of the experiment in Ref. [15]. In one layer we fix the number of IXs to $N_1 = 4$ and vary the number of IXs in the other layer N_2 from 1 to 8. It should be noted, that due to the 1D character and small sizes of the systems considered here, we will not be able to achieve quantitative agreement with the experiments. Our goal here is rather to gain a qualitative understanding of the physical characteristics of the system. In particular, we would like to understand the nonmonotonous dependence of the interlayer binding energy on the single layer IX density observed in Ref. [15].

Figure 7(a) shows the dependence of the energy per IXs on the number of particles in the second layer N_2 for different values of the hopping amplitude. As can be seen from the figure, the energy per IXs in the calculations with interlayer

interaction has a minimum when $N_2 = N_1 = 4$. This minimum is not present when the interlayer interaction is switched off. Addition of hopping deepens and smoothens out the minimum and, for large hopping amplitudes, can even shift the minimum towards smaller values of N_2. Similarly, the minimum can be pushed to larger values of N_2 by increasing a. This demonstrates the competition between three energy scales: The intralayer interaction, the interlayer interaction, and the hopping energy.

The energy minimum for $N_1 = N_2$ in Fig. 7 reproduces very well the one observed in the experimental results (cf. Fig. 5 of Ref. [15]), which appears when the IX densities are approximately equal for both IX bilayers. The appearance of the minimum energy in the experiments of Ref. [15] at $N_1 \simeq N_2$ therefore suggests the following hierarchy of energy scales: The short-range intralayer interaction is the largest energy scale when compared to interlayer interaction, whereas the hopping contribution is negligible as compared to the other two energy scales. The IXs tend, therefore, to arrange themselves equidistantly in both bilayers by sitting on top of each other. This is reminiscent of crystalline phases observed for dipolar bosons in other contexts [29–31]. The minimum energy is thus achieved when IX density is the same in both bilayers. The fact that the energies in Fig. 7(a) for cases with and without interlayer interaction do not approach each other for large N_2 is a characteristic property 1D systems. Contrary to the 2D case, where the integrated interlayer interaction between an IX and an infinite homogeneous distribution of IX vanishes, the interaction between an IX and an infinite line of dipoles is not zero. One has, therefore, a finite interlayer contribution in 1D systems, which does not grow with N_2.

We next consider the interlayer pair correlation function $g_{12}(x)$ [cf. Fig. 7(b)], which yields information about the distribution of IXs in the layer system. This figure clearly shows that when the interlayer interaction is turned on the pair correlation function at $x = 0$ becomes larger than one, which demonstrates that the probability of occupation of the same position in both layers is preferred. Increasing hopping amplitude reduces the peak value at $x = 0$ essentially suppressing same site occupation in two layers, which again demonstrates the competition between the two energy scales.

Another way to understand the position of the minimum in Fig. 7(a) is to consider the structure factor for the system. Figure 8 shows both the intralayer and interlayer structure factor for two values for the number of IXs in the second layer $N_2 = 4$ and $N_2 = 6$. For the case $N_2 = 4$, both intralayer and interlayer structure factors show a peak when $q = 4$, which signalizes the presence of short range order in the system. The fact that the peaks in the two plots appear for the same q's shows that intra- and interlayer interactions are completely balancing each other and the system is its lowest energy state. When $N_2 = 6$, while the first layer structure factors S_{11} still retain the peak at $q = 4$, the peak for the second layer S_{22} and interlayer S_{12} structure factors shifts from the $q = 4$ position. Therefore, in this case there is an imbalance between the two energy scales and intralayer interaction determines the distribution of IXs in both layers. A similar suppression of the peaks in the structural factor as well as in the pair-correlation functions is observed when the hopping amplitude is increased (not shown).
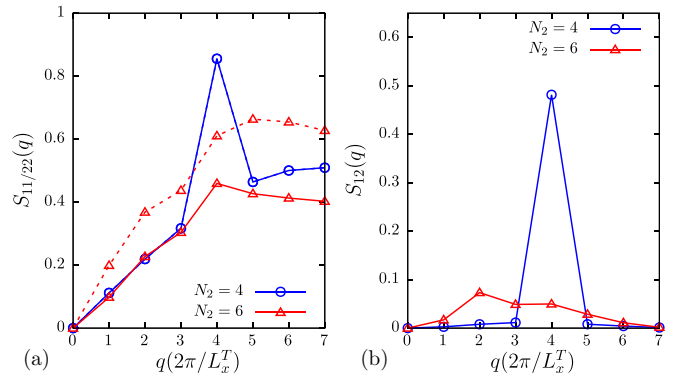

FIG. 8. (a) Intralayer structure factor for two cases of number of IXs in the second layer. Solid (dashed) lines correspond to $S_{11}(q)$ $(S_{22}(q))$. $S_{11}(q)$ and $S_{22}(q)$ are the same when $N_1 = N_2$. (b) interlayer structure factor for two cases of number of IXs in the second layer. The hoping amplitude is set to $t = 2.0$ in both figures.

In conclusion, the results of this section reproduce the experimentally observed nonmonotonous dependence of the IX energies on the one layer IX density shown in Ref. [15]. They also show that the minimal energy per particle in stacked 1D bilayers is achieved for equal densities in both bilayers with the IXs in one bilayer aligned with those in the other one to maximize the attractive component of the dipolar coupling.

C. IX dipolaron

The previous sections have addressed models for interlayer excitonic interactions based on the arrangement of the particles on fixed lattice sites. The interaction between the single IX in DQW$_2$ and the lattice may also deform the IX lattice, thus leading to formation of an IX dipolaron with increased interaction energy. This section discusses dipolaron models for the dipolar interaction between IXs.

1. IX Lattice Dipolaron

We first consider a lattice dipolaron arising from the distortion of the IX lattice in DQW$_1$ shown in Fig. 6(a). Due to the large values of the repulsive intra-DQW interaction in comparison with the attractive inter-DQW interaction, it is not obvious whether dipolaron formation is energetically favorable. In fact, an IX molecule cannot bind an additional IX because the intra-DQW repulsive forces on the extra IX always exceed the attractive inter-DQW attraction [cf. Fig. 1(c) and Ref. [16]]. In a locally deformed lattice, in contrast, the increased repulsion experienced by an IX when it approaches one of its neighbors is partially compensated by the reduction in repulsion as it moves away from the neighbors on the opposite side. This compensation mechanism enables the attractive inter-DQW to reduce the electrostatic energy and stabilize the dipolaron.

The dipolaron formation energy was calculated for the triangular lattice shown in the inset of Fig. 9 by assuming that the neighbors of the central IX (i.e., the one aligned with the single IX in DQW$_2$) can displace radially by an amount $\epsilon_{r_\parallel} L_x$, where $\epsilon_{r_\parallel}$ is given by the Ansatz form:

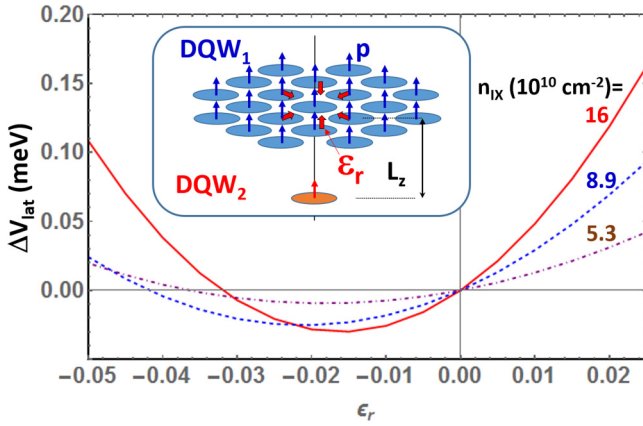$$\epsilon(r_\parallel) = \epsilon_r e^{-[\frac{r_\parallel - L_x}{r_\epsilon}]}, \quad r_\parallel > 0. \tag{11}$$

FIG. 9. Dependence of the energy changes ΔV_{lat} of a single IX in DQW$_2$ on the deformation ϵ_r of the closed-packed triangular lattice of IX in DQW$_1$ displayed in the inset. The calculations were carried out for $L_z = 36$ nm and lattice constants L_x corresponding to IX densities $n_{\text{IX}} = 2/(\sqrt{3}L_x^2)$ listed in the figure.

Here, $\epsilon(r_\parallel)$ yields the relative radial displacement of the IXs at a distance $r_\parallel$ from the center of the dipolaron, $\epsilon_r r_\parallel$ is the lateral decay length of the deformation, and ϵ_r the relative displacement of the first neighbors of the central IX located at $r = L_x$. According to the definition in Eq. (11), ϵ_r corresponds to the relative displacement of the nearest neighbors.

Figure 9 shows the effect of the deformation on the potential experienced by the single IX (quantified in terms of the energy difference $\Delta V_{\text{lat}} = V_{\text{lat}}(0,0,\epsilon_r) - V_{\text{lat}}(0,0,\epsilon_r = 0)$ introduced by the deformation ϵ_r) as a function of the lattice density. The minima of $\Delta V_{\text{lat}}(\epsilon_r)$ occur for $r_\epsilon \ll L_x$, thus indicating that the deformation is restricted to the first neighbors. For this reason, the subsequent calculations were carried out assuming that the deformation is restricted to the first ring of IXs around the single IX in DQW$_2$. The plots show that the total energy reduces for small negative deformations (on the other of a few %), which arise from the attraction of the neighbors by the single IX.

Figure 10 displays the equilibrium values for ϵ_r and ΔV_{lat} obtained by minimizing the lattice energy for different lattice densities. The minimum in ΔV_{lat} for large lattice distances occurs for a ratio $L_x/L_z \approx 1/3$. This result is consistent with the increase of the inter-DQW attractive potential with respect to the repulsive one (cf. Fig. 3) in this parameter range. As a result, the total energy reduces if the first neighbors approach the central IX (i.e., for negative values of ϵ_r). The change in sign of of ϵ_r for decreasing densities is related to the fact interaction energy U_t (cf. Fig. 3) also changes sign and becomes positive when $L_x > L_z/\sqrt{3}$.

The potential acting on the single IX in DQW$_2$ calculated at the minimum of Fig. 10 are displayed in Fig. 11. The lattice deformation (of a few %) required for dipolaron formation is quite small. Also, the energy gain only reaches a few tens of μeV and is thus smaller than the typical spectral width of IX lines (on the order of a meV). The dipolaron binding energy may be increased by increasing the IX dipole length or decreasing the spacing between the DQWs. The changes, however, are not expected to be drastic. As an example, we
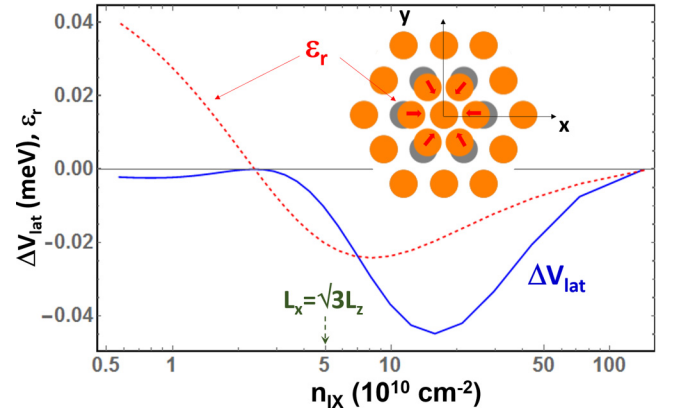
estimated that a reduction of the DQW spacer from 10 nm to 8 nm enhances the dipolaron binding energy by approx. 30%.

FIG. 10. Equilibrium values for the deformation (ϵ_r) and corresponding change in potential (ΔV_{lat}) as a function of lattice density n_{IX}. The orange circles in the inset show the deformation of the originally triangular IX lattice (gray circles) due to dipolaron formation around the central site bound to an IX in the adjacent DQW layer.

2. Continuous dipolaron

The interaction between a single IX in DQW$_2$ and the excitonic liquid in DQW$_1$ in the inset of Fig. 6 can be also described in terms of a continuous, Fröhlich-type dipolaron, as given by the following Hamiltonian [32]:

$$\hat{H} = \frac{\hat{\mathbf{p}}^2}{2M} + \sum_{\mathbf{k}} \hbar\omega(k)\hat{b}_{\mathbf{k}}^\dagger \hat{b}_{\mathbf{k}} + \sum_{\mathbf{k}} U(k)(e^{-i\mathbf{k}\hat{\mathbf{r}}}\hat{b}_{\mathbf{k}}^\dagger + e^{i\mathbf{k}\hat{\mathbf{r}}}\hat{b}_{\mathbf{k}}),$$

(12)

with $\sum_{\mathbf{k}} = (2\pi)^{-2}\int d^2k$. The first term of Eq. (12) describes the single excitonic "impurity" in DQW$_2$ with momentum $\hat{\mathbf{p}}$ and mass M; the second term gives the kinetic energy of the bosonic excitations (e.g., phonons) in the DQW$_1$ exciton liquid, as parametrized by the dispersion relation $\omega(k)$; and
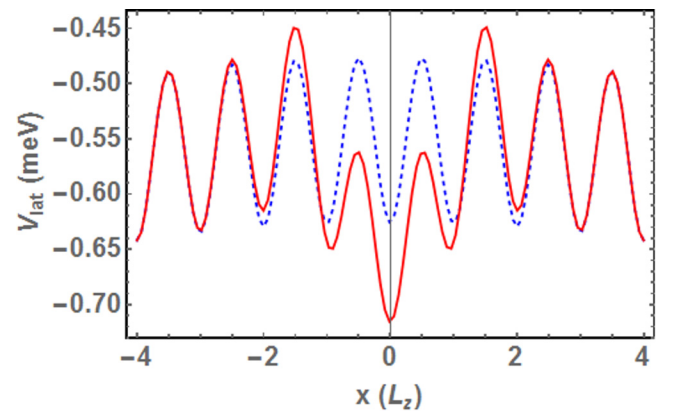

FIG. 11. Potential landscape across an IX dipolaron. The solid line displays the IX potential calculated along the x direction of the IX lattice dipolaron displayed in the inset of Fig. 10. The calculations were carried out for the structure in the upper inset of Fig. 9 with $L_x = 27.7$ nm, which corresponds to the minimum for ΔV_{lat} in Fig. 10.

the last term represents the impurity-boson interactions. The momentum-space interaction parameter, $U(k)$, can be represented as

$$U(k) = f(k)V(k). \tag{13}$$

Here,

$$V(k) = \int d^2 r U_{dd}(r) e^{-i\mathbf{kr}} = -\mu^2 \pi k \, e^{-kL} \tag{14}$$

is the Fourier transform of the two-body interaction potential $U_{dd}(r)$ given by Eq. (1) and μ is defined in Eq. (6). The function $f(k) = [n_{IX}\varepsilon(k)/(\hbar\omega(k))]^{1/2}$ depends on the density n_{IX}, single-particle energy $\varepsilon(k) = \hbar k^2/(2m)$ as well as on the correlation state of the IX gas expressed in terms of its dispersion relation $\hbar\omega(k)$. $m = m_e + m_{hh}$ is the exciton mass.

If the excitonic impurity in DQW_2 is static, it corresponds to an "infinite-mass dipolaron", $M = \infty$ (we set the excitonic impurity at $\mathbf{r} = 0$, for convenience). In this case, the Hamiltonian in Eq. (12) can be exactly diagonalized using a coherent-state transformation

$$\hat{S} = \exp\left[-\sum_{\mathbf{k}} \frac{U(k)}{\hbar\omega(k)} (\hat{b}_{\mathbf{k}}^{\dagger} - \hat{b}_{\mathbf{k}})\right], \tag{15}$$

which gives the following ground-state energy shift:

$$\Delta E_{IX} = -\sum_{\mathbf{k}} \frac{U(k)^2}{\hbar\omega(k)}. \tag{16}$$

The corresponding ground eigenstate is given by $|\psi\rangle = \hat{S}|0\rangle$, where $|0\rangle$ is the boson vacuum. Equation (16) gives a deformation energy of DQW_1 due to the interaction with a single exciton in DQW_2. In the case of a Hamiltonian with a linear coupling, such as Eq. (12), the deformation energy is always negative, thus yielding a stable dipolaron phase.

The ground state energy in Eq. (16) depends on the correlation state of the IX fluid. Let us consider two limiting cases depending on the fluid density in DQW_1: That of a low-density noninteracting exciton gas and of a high-density interacting exciton liquid. For a noninteracting exciton gas, the dispersion relation is that of free particles, $\hbar\omega(k) \equiv \varepsilon(k) = \hbar^2 k^2/(2m)$, thus resulting in a deformation energy given by

$$\Delta E_{IX} = -n_{IX}\mu^4 \frac{\pi m}{\hbar^2 L_z^2}. \tag{17}$$

For an interacting exciton gas or liquid, the dispersion relation can be stated as $\omega(k) \sim c(n_{IX})k$, where $c(n_{IX})$ is the speed of sound in the IX fluid, which depends on the density n_{IX}. One then obtains

$$\Delta E_{IX} = -n_{IX}\mu^4 \frac{3\pi}{8L_z^4 mc^2(n_{IX})}. \tag{18}$$

In the regime of Bogoliubov excitations, $c(n_{IX}) \sim \sqrt{n_{IX}}$, so that ΔE_{IX} becomes density-independent. The numerical computations of Ref. [33] revealed that the exciton liquid is strongly-interacting yielding $c(n_{IX}) \sim n_{IX}^{0.7}$ (see Fig. 3(b) of Ref. [33]). One then obtains an energy shift $\Delta E_{IX} \sim -n_{IX}^{-0.4}$ with magnitude decreasing with increasing density.

The solid and dotted lines in Fig. 6 compare the deformation energies predicted by Eqs. (17) and (18), respectively, with the lattice dipolaron model discussed in Sec. IV C 1.
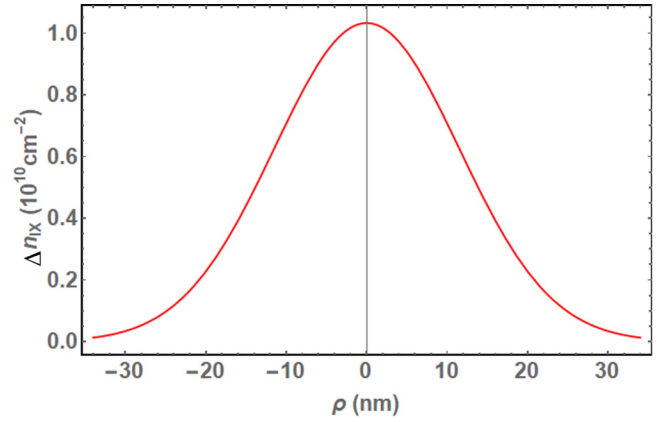

FIG. 12. Dipolaron density profile Δn_{IX} determined from Eq. (19) for a fluid density $n_{IX} = 10^{10}$ cm^{-2} and $L_z = 34$ nm.

One can see that the results for a correlated exciton liquid, Eq. (18), are in good agreement with the lattice model at large densities n_{IX}. The latter is consistent with the fact that the lattice model presupposes correlations in displacements of the IX within the lattice. The uncorrelated model (solid line in Fig. 6) gives, in contrast, much larger energy redshifts $|\Delta_{IX}|$ with increasing densities. The interlayer binding energies predicted by the model for densities in the range $5 \times 10^{10} - 10^{11}$ are indeed comparable to the experimentally measured ones [15]. This agreement is, however, surprising since the high interlayer binding energies partially arise from the fact that the dipolaron model assumes a free-particle IX dispersion and, thus, neglects repulsive intra-DQW interactions, which are expected to become important with increasing densities.

In real space, the density deformation of DQW_1 is given by $\Delta n_{IX}(\rho) = \langle\psi|\hat{b}_{\mathbf{r}}^{\dagger}\hat{b}_{\mathbf{r}}|\psi\rangle$, where $\hat{b}_{\mathbf{r}}^{\dagger} = \int d^2k/(2\pi)^2 \hat{b}_{\mathbf{k}}^{\dagger} e^{i\mathbf{k}\rho}$ and $\rho = \mathbf{r}_{\parallel}$. In the case of a correlated exciton fluid in DQW_1, the density deformation $\Delta n_{IX}(\rho)$ at small values of ρ can be approximated by a Gaussian curve given by

$$\Delta n_{IX}(\rho) = n_{IX}\frac{\mu^4}{2\hbar mc^3(n_{IX})}\frac{9\pi}{16L_z^5}e^{-\frac{\rho^2}{2\sigma^2}}, \tag{19}$$

where $\sigma = 2L_z/\sqrt{35}$. Note that the spatial extension of the dipolaron cloud only depends on the inter-DQW spacing L_z while the amplitude of the fluctuations reduce with increasing density n_{IX}. For the experimental conditions of Ref. [15] with $L_z = 34$ nm, the full width at half maximum of the deformation is 27 nm, as illustrated in Fig. 12. The fluid density almost doubles at the lateral position of the single IX. By integrating Δn_{IX} over the DQW plane one obtains a total density excess corresponding to approx. 0.1 particles for $n_{IX} = 10^{10}$ cm^{-2}.

V. CONCLUSIONS

We have theoretically investigated dipolar polarization effects in the interaction between IXs in stacked DQW structures. The dipolar inter-DQW coupling in these structures turns from repulsive for large lateral distances between the IXs to attractive for short separations. The attraction enables the bonding of the IXs into an IX-molecule with a binding

energy of a few hundreds of μeV [16], as calculated in the PCA for the IX dipoles. We show that the dipolar inter-DQW interaction deforms the wave function of the electron and hole constituents of the excitons with two main consequences: An increase in the IX interlayer binding energy (by approximately 20%) as well as a dependence on the dipole moment on the amplitude of the applied field, thus yielding a finite IX polarizability.

We have also analyzed multiparticle effects in the inter-DQW dipolar interaction by considering the coupling between a single IX in one of the DQWs to a (static) close-packed lattice of IXs in the other DQW. For this configuration, the interlayer binding energy of the single IX reduces with increasing lattice density. This behavior is due to the dominating role of the intra-DQW dipolar repulsion, which prevents more than one IX entering the attractive region of the inter-DQW coupling. We also found that the inter-DQW attraction can create a distortion of the lattice, thus forming an IX dipolaron and increasing the IX interlayer binding energy. The lattice model was found to be in good agreement with the theory for a continuous, Fröhlich-like dipolaron in the correlated regime. This is not surprising due to the correlated nature of the dipolar interactions of the lattice models. In the low IX density, uncorrelated regime, the Fröhlich-like dipolaron model also accounts for the regime, where the measured interlayer binding energy increases with density. The simple approxima-

tion presented here neglects, however, intra-DQW interactions and can, thus, only be regarded as a rough approximation for the density regime in the transition from uncorrelated to correlated behavior. In fact, the interplay between the dipolar and the short-range exchange interactions at high particle densities has been recently shown to lead to the formation of mixed dark and bright condensed Bose phases with interesting physics of interacting quantum liquids [27,34–37]. We expect nevertheless that the results presented here will stimulate further experimental and theoretical studies of dipolar inter-DQW interactions in IX systems consisting of DQW stacks.

[1] T. Lahaye, C. Menotti, L. Santos, M. Lewenstein, and T. Pfau, Rep. Prog. Phys. **72**, 126401 (2009).

[2] H. Kadau, M. Schmitt, M. Wenzel, C. Wink, T. Maier, I. Ferrier-Barbut, and T. Pfau, Nature (London) **530**, 194 (2016).

[3] T. Lahaye, T. Koch, B. Frohlich, M. Fattori, J. Metz, A. Griesmaier, S. Giovanazzi, and T. Pfau, Nature (London) **448**, 672 (2007).

[4] L. Santos, G. V. Shlyapnikov, and M. Lewenstein, Phys. Rev. Lett. **90**, 250403 (2003).

[5] L. Chomaz, R. M. W. van Bijnen, D. Petter, G. Faraoni, S. Baier, J. H. Becher, M. J. Mark, F. Wächtler, L. Santos, and F. Ferlaino, Nat. Phys. **14**, 442 (2018).

[6] T. Doiron-Leyraud, Physics **12**, 38 (2019).

[7] F. Böttcher, J.-N. Schmidt, M. Wenzel, J. Hertkorn, M. Guo, T. Langen, and T. Pfau, Phys. Rev. X **9**, 011051 (2019).

[8] L. Tanzi, E. Lucioni, F. Famà, J. Catani, A. Fioretti, C. Gabbanini, R. N. Bisset, L. Santos, and G. Modugno, Phys. Rev. Lett. **122**, 130405 (2019).

[9] L. Chomaz, S. Baier, D. Petter, M. J. Mark, F. Wächtler, L. Santos, and F. Ferlaino, Phys. Rev. X **6**, 041039 (2016).

[10] J. P. Eisenstein and A. H. MacDonald, Nature (London) **432**, 691 (2004).

[11] J. P. Eisenstein, Ann. Rev. Condens. Matter Phys. **5**, 159 (2014).

[12] L. V. Butov, L. S. Levitov, A. V. Mintsev, B. D. Simons, A. C. Gossard, and D. S. Chemla, Phys. Rev. Lett. **92**, 117404 (2004).

[13] R. Rapaport, G. Chen, D. Snoke, S. H. Simon, L. Pfeiffer, K. West, Y. Liu, and S. Denev, Phys. Rev. Lett. **92**, 117405 (2004).

[14] J. Rudolph, R. Hey, and P. V. Santos, Phys. Rev. Lett. **99**, 047602 (2007).

[15] C. Hubert, Y. Baruchi, Y. Mazuz-Harpaz, K. Cohen, K. Biermann, M. Lemeshko, K. West, L. Pfeiffer, R. Rapaport, and P. Santos, Phys. Rev. X **9**, 021026 (2019).

[16] K. Cohen, M. Khodas, B. Laikhtman, P. V. Santos, and R. Rapaport, Phys. Rev. B **93**, 235310 (2016).

[17] L. A. P. Ardila and T. Pohl, J. Phys. B: At., Mol. Opt. Phys. **52**, 015004 (2018).

[18] J. C. Slater and G. F. Koster, Phys. Rev. **94**, 1498 (1954).

[19] P. Vogl, H. P. Hjalmarson, and J. D. Dow, J. Phys. Chem. Solids **44**, 365 (1983).

[20] K. C. Hass, H. Ehrenreich, and B. Velický, Phys. Rev. B **27**, 1088 (1983).

[21] D. J. Chadi, Phys. Rev. B **16**, 790 (1977).

[22] L. C. Lew Yan Voon and L. R. Ram-Mohan, Phys. Rev. B **47**, 15500 (1993).

[23] J. N. Schulman and Y.-C. Chang, Phys. Rev. B **31**, 2056 (1985).

[24] Y. Takahashi, Y. Kato, S. S. Kano, S. Fukatsu, Y. Shiraki, and R. Ito, J. Appl. Phys. **76**, 2299 (1994).

[25] V. Arsoski, N. ukari, M. Tadi, and F. Peeters, Comput. Phys. Commun. **197**, 17 (2015).

[26] B. Laikhtman and R. Rapaport, Phys. Rev. B **80**, 195313 (2009).

[27] Y. Mazuz-Harpaz, K. Cohen, M. Leveson, K. West, L. Pfeiffer, M. Khodas, and R. Rapaport, Proc. Natl. Acad. Sci. USA **116**, 18328 (2019).

[28] M. Remeika, J. Leonard, C. Dorow, M. Fogler, L. Butov, M. Hanson, and A. Gossard, in *Conference on Lasers and Electro-Optics* (Optical Society of America, Washington, DC, 2016), p. JW2A.97.

[29] R. A. Suris, J. Exp. Theor. Phys. **122**, 602 (2016).

[30] X. Lu, C.-Q. Wu, A. Micheli, and G. Pupillo, Phys. Rev. B **78**, 024108 (2008).

[31] F. Cinti, D.-W. Wang, and M. Boninsegni, Phys. Rev. A **95**, 023622 (2017).

[32] J. T. Devreese, arXiv:1012.4576.

[33] Y. E. Lozovik, I. Kurbakov, G. Astrakharchik, J. Boronat, and M. Willander, Solid State Commun. **144**, 399 (2007).

[34] A. A. High, J. R. Leonard, A. T. Hammack, M. M. Fogler, L. V. Butov, A. V. Kavokin, K. L. Campman, and A. C. Gossard, (London) **483**, 584 (2012).

[35] M. Combescot, R. Combescot, and F. Dubin, Rep. Prog. Phys. **80**, 066501 (2017).

[36] M. Stern, V. Umansky, and I. Bar-Joseph, Science **343**, 55 (2014).

[37] K. Cohen, Y. Shilo, K. West, L. Pfeiffer, and R. Rapaport, Nano Lett. **16**, 3726 (2016).